15B.1

THE IMPACT OF ELEVATION SCAN SPACING OBSERVATIONS OF HEAT BURSTS SAMPLED BY THE NATIONAL WEATHER RADAR TESTBED PHASED ARRAY RADAR

Adam J. Smith[1 *], Phillip B. Chilson[1], Pamela L. Heinselman[2]

[1]*Atmospheric Radar Research Center and School of Meteorology, University of Oklahoma, Norman, OK*

[2]*NOAA/OAR National Severe Storms Laboratory, Norman, OK*

1. INTRODUCTION

In the wake of some nocturnal thunderstorms, surface locations may experience a sudden increase in temperature, a simultaneous decrease in dew point temperature, and gusty winds. These events, known as “heat bursts” (Johnson 1983), are typically observed during the Spring months in the Great Plains of the United States. Heat bursts are believed to be rare, having only been observed 203 times by the Oklahoma Mesonet over a 14.5 year period (McPherson et al. 2008). The small spatial scale of these phenomena makes them difficult to detect by surface observation stations. However, heat bursts are significant because they can produce severe wind gusts. On 23 June 1996, heat bursts contributed to wind gusts up to 47 m s^{-1} (MacKeen et al. 1998). These winds produced more than \$18 million in damage over a 40,000 km^2 region of southwest Oklahoma. Temperatures during this event reached 40°C, creating a danger for persons and livestock sensitive to extreme heat.

Due to the severe winds and high temperatures generated by heat bursts, reasonable warning must be provided to determine when and where these events will occur. High sampling rates are needed to better resolve the rapid development and evolution of features in the storm’s vicinity. Also, multiple theories of heat burst development have been advanced (Johnson 1983; Bernstein and Johnson 1994), but the mechanisms behind the initial onset of heat bursts are not well understood. Thus, observations of heat bursts must be analyzed to determine why heat bursts develop, and how strong they could potentially become. These observations need to provide sufficient vertical detail to fully resolve the precipitation and wind velocity structure within the storm.

During the Spring of 2009, the National Weather Radar Testbed (NWRT) Phased Array Radar (PAR) in Norman, Oklahoma (Zrnic et al. 2007) was used to evaluate new scanning techniques for weather radar observations. As part of the Phased Array Radar Innovative Sensing Experiment (PARISE; Heinselman et al. 2009), a “dense” scanning strategy was developed containing 25 elevations. This strategy provided a complete 90° azimuthal volume with an update rate of approximately 2 min, allowing for detailed analysis of vertical storm structure while obtaining frequent updates for tracking storm evolution.

On the evening of 13 May 2009, the dense scanning strategy was used to sample an MCS that produced heat bursts over a large region of southwest and central Oklahoma. The storms were sampled for a period of 2.5 hours as they moved toward the NWRT PAR, allowing for a detailed study of heat burst activity. Data from the National Weather Service’s Weather Surveillance Radar-1988 Doppler (WSR-88D) network were obtained continually throughout the event, allowing for comparison with NWRT PAR data. The WSR-88D returns also provide a means of analysis when the NWRT PAR was not sampling.

This paper provides a detailed analysis of the 13 May 2009 heat burst event using radar data from two WSR-88Ds and the NWRT PAR. Heat bursts are detected using surface observations of temperature, dew point temperature and wind obtained from the Oklahoma Mesonet (McPherson et al. 2007).

**Corresponding author address*: Adam J. Smith, Atmospheric Radar Research Center and School of Meteorology, 120 David Boren Dr., Suite 4636, Norman, OK 73072-7307; *e-mail: adam.j.smith-1@ou.edu.*

All radar and Mesonet data are displayed using the Warning Decision Support System – Integrated Information (WDSS-II; Lakshmanan et al. 2007). WSR-88D data from Frederick, OK (KFDR) and Twin Lakes, OK (KTLX) are used to analyze the initial heat burst activity over the Texas panhandle and southwestern Oklahoma. Vertical cross sections of NWRT PAR and KTLX data are examined to determine the cause of the later heat bursts over central Oklahoma. Results from NWRT PAR and KTLX are compared to determine the benefit of improved vertical sampling when compared to current WSR-88D scanning strategies.

2. DESCRIPTION OF NWRT PAR AND WSR-88D SCANNING STRATEGIES

The NWRT PAR "dense" vertical scanning strategy uses 25 closely spaced elevations that overlap up to one-half beamwidth. This design allows for high vertical resolution observations of storm structure while limiting elevation gaps. The resolution provided by this strategy is useful for sampling hail storms and other events where vertical structure is important. A continuous 90° sector may be sampled in approximately 2 min, whereas a 60° sector reduces the update time by a factor of one-third.

Two scanning patterns were developed to account for target range from the radar. A "near" scan (Fig. 1) is used to sample targets within 80 km of the radar. This scan also provides vertical coverage up to 15 km AGL for targets farther than 35 km from the radar. A second pattern, the "far" scan (Fig. 2), is used to sample targets farther than 80 km from the radar. The far scan spaces the elevation angles closer together, so it is also useful for providing greater vertical resolution in cases with low-topped targets that are close to the radar. A list of elevation angles and the specifications used in each scanning pattern is provided in Tables 1 and 2.

The NWRT PAR is a single-faced, electronic scanning radar that allows for agile-beam scanning of weather features (Zrnic et al. 2007). Being a research radar, the NWRT PAR has some limitations. Due to the current antenna design, the beamwidth broadens when scanning off antenna broadside. Thus, the dense scanning strategy scans a maximum azimuthal sector of 90°. Also, the PAR antenna provides less sensitivity than a WSR-88D antenna. In several instances during the 13 May heat burst event, some features are not fully observed as they are outside the azimuthal scanning sector. Operational phased array systems, such as military radars, use multiple antenna faces to scan a complete 360° volume (Sensi 1988). Additional antenna faces with more sensitivity are likely to be included in a future Multifunction PAR prototype (National Academies 2008; Weadon et al. 2009).

The WSR-88Ds use a variety of Volume Coverage Patterns (VCPs) based on storm type and forecaster preference. Specifications for each VCP are provided in Federal Meteorological Handbook (2009). For this study, the KFDR WSR-88D used VCPs 11 and 212, while KTLX used VCP 11. Due to variations in elevation scans and other settings, the update rates for the VCPs range from 4.5 to 5 min. Therefore, the WSR-88D temporal update rate is relatively consistent throughout the entire heat burst event.

3. DISCUSSION OF HEAT BURST MECHANISMS AND RADAR SIGNATURES

Two conceptual models have been developed to explain heat burst formation in the vicinity of a mesoscale convective system (MCS; Johnson 2001). Both of these mechanisms require a nearly dry-adiabatic lapse rate to allow downdrafts to accelerate and warm rapidly. A shallow surface inversion allows sufficiently strong downdrafts to overshoot their equilibrium level and reach the surface (Johnson 1983). Strong downdrafts are typically associated with dissipating convection. Thus, heat bursts are often observed after sunset, when diurnal convection typically begins to weaken (McPherson et al. 2008).

One mechanism for developing heat bursts is via a microburst. Johnson (1983) discusses downdrafts that are induced by evaporative cooling at the base of a stratiform region. The cool air warms and accelerates as it descends dry-adiabatically. Precipitation in the vicinity of the downdraft will evaporate quickly, decreasing the dew point temperature of the air parcel. A radar signature of a microburst may consist of midlevel convergence within the stratiform region that descends rapidly toward the surface (Wilson et al. 1984). Depending on the temporal sampling rate, the descent may be visible over two or more volume scans. Divergence may also be visible near the ground if the target is sufficiently close to the radar. In addition, a bounded region of lower reflectivity may be present within higher reflectivity, indicating evaporation in the vicinity of the microburst. Since microbursts may form either ahead of or behind a progressing MCS, adequate vertical resolution must be obtained in order to detect the downburst and nearby regions of evaporation. Also, since heat bursts can develop in approximately 5 min (Bernstein and Johnson 1994), a volume scan must provide adequate temporal resolution to detect the onset of rapidly descending flow.

In addition to the microburst mechanism, Bernstein and Johnson (1994) discuss heat burst initiation due to a rear-inflow jet. In this scenario, storm-relative inflow develops beneath the rear stratiform region of the MCS. As this inflow approaches the rear of the MCS precipitation region, the flow turns downward due to evaporative cooling in the vicinity of the precipitation core. Convergence between the rear-inflow jet and storm-relative outflow may also enhance a downdraft. Near the ground, the downdraft is forced outward as it encounters the ground. Thus, a radar signature of a rear-inflow heat burst would be convergence aloft (4–5 km AGL) along with storm-relative outflow or divergence near the surface. In many cases, a weak reflectivity region may appear just to the rear of the downdraft, indicating water vapor that is captured by the downdraft, evaporates as the air warms, and then condenses as the air cools in the moist inversion layer. Similar to the downburst mechanism, the rear-inflow heat burst can develop quickly (Bernstein and Johnson 1994), so a rapid scan rate is necessary to fully sample the evolution of this feature. Also, elevation coverage must be closely spaced to ensure that all features are well-observed.

4. SYNOPTIC AND ENVIRONMENT OVERVIEW

A surface analysis from 0000 UTC 13 May 2009 indicates a stationary front extending north-to-south across western Nebraska and Kansas, then south-southeastward across western Oklahoma and eastward across southern Oklahoma (not shown). A dryline was also oriented north-to south over the Texas panhandle. Temperatures ranged from near 31°C in southwest Oklahoma to 18°C in far northeast Oklahoma. High relative humidities were also present across Oklahoma and into the Texas panhandle.

A sounding from Norman, Oklahoma at 0000 UTC on 13 May 2009 (Fig. 3) shows a deep dry layer from 800 to 300 hPa. This dry layer was conducive to evaporation of precipitation as it descended. In turn, the evaporation helped contribute to downdrafts, as described by Johnson (1983). Also, a nearly dry-adiabatic lapse rate existed from near 800 hPa to 475 hPa. This lapse rate allowed downdrafts to warm more rapidly than the surrounding environment, leading to acceleration and further evaporation. Finally, a temperature inversion extended from the surface to approximately 800 hPa. This shallow inversion may be penetrated by sufficiently strong downdrafts. All of these features closely match features noted by Johnson (1983) as conditions favorable for heat burst formation.

5. MCS EVOLUTION AS DEPICTED BY WSR-88D

Two thunderstorm clusters developed along the dryline in western Texas prior to 2200 UTC 12 May 2009 (not shown). As the storms intensified over the southeastern Texas panhandle (0040 UTC 13 May), they produced a strong heat burst at Childress, Texas (KCDS; Fig. 4). This heat burst produced severe wind gusts over 25 m s^{-1} and also induced a 5-min dew point depression of 15°C. At 0037 and 0042 UTC, a narrow precipitation band existed in the vicinity of Childress (Fig. 5). Shortly thereafter, a region of drying developed directly above KCDS (0047–0052 UTC). These regions of drying indicate locations where evaporation may be occurring in the vicinity of a heat burst. Fig. 6 shows weak storm-relative outflow over KCDS (0042 UTC), but midlevel convergence and near-surface divergence are not apparent. Due to Childress' range from KFDR and the scanning strategy being used (VCP 11), the elevation beamwidth of the radar was too wide to provide sufficient information on the velocity and reflectivity structures of the microburst. In this situation, overlapped elevation scans may provide additional information on the reflectivity and velocity structure that contributed to a heat burst. Thus, a scanning strategy with closely spaced elevation scans may provide the vertical detail needed to understand the conditions observed at this location.

As the storms moved northeastward into Oklahoma, the two storm clusters remained distinct, with a narrow band of showers between them. At 0200 UTC, the southern storm remained in northwest Texas, while the northern cluster moved into southwest Oklahoma. A 45-min sustained heat burst was observed at Erick, Oklahoma (ERIC) starting at 0210 UTC (Fig. 7). Reflectivity (Fig. 8, panel a) shows a region of precipitation directly above ERIC, with a stratiform region aloft and to the northwest. Reflectivities near 40 dBZ indicate the location of the main precipitation core. Storm-relative velocity (Fig. 8, panel b) also shows a rear-inflow jet extending from northwest to southeast at 4–5 km AGL. This rear-inflow jet converged with storm-relative outflow aloft, likely inducing a downdraft. Closer to the ground, weak outflow is visible just to the west of ERIC, showing that the downdraft may have reached the ground and spread outward. These signatures provide evidence that a rear-inflow heat burst occurred at this location. During this time, KFDR used VCP 212, which consists of three closely spaced elevation scans near the ground. Data from these elevation scans provide more useful detail on storm structure when compared to VCP 11. However, due to range from the radar, the scan could not provide information on the horizontal extent of the near-surface outflow. This information is important when forecasting the location and duration of a heat burst event. Also, only the lowest three elevation scans were closely spaced, so the vertical resolution is not equal for all elevation scans.

Meanwhile, the southern cluster of thunderstorms moved northeastward into Oklahoma by 0300 UTC. The first heat burst observed with this cluster occurred at Altus, Oklahoma at 0318 UTC (Fig. 9). KFDR reflectivity (Fig. 10, panel a) reveals that the rear of the precipitation region was just east of Altus, providing a possibility that the rear-inflow heat burst mechanism may be present . Like the Erick heat burst, storm-relative velocity (Fig. 10, panel b) indicates a rear-inflow jet that reached the edge of the precipitation core at 4 km AGL. Weak convergence appears at this location, and strong outflow is observed near the surface. These features indicate that a rear-inflow heat burst signature is present and well-defined in this radar scan. Since the storm was less than 20 km from KFDR, the elevation beam width was sufficiently small to resolve the small-scale features of the heat burst. However, for targets at longer ranges from the radar, similar structures may not be observed.

6. COMPARISON OF PAR AND WSR-88D RETURNS

After 0330 UTC, the NWRT PAR began scanning the event using the dense vertical sampling strategy. Two heat bursts were observed at Bessie and Weatherford, Oklahoma between 0330 UTC and 0400 UTC (not shown). Both of these sites are farther than 110 km from both NWRT PAR and KTLX. Thus, velocity range folding prevented a complete view of storm structures. However, another heat burst signature provided an opportunity to compare both the vertical resolution and temporal resolution obtained by the two radars.

At 0412 UTC, a bounded area of weak reflectivity echoes appears to the northeast of Medicine Park, Oklahoma (MEDI) on both NWRT PAR and KTLX (Fig. 12). From 0412–0417 UTC, this precipitation evaporated, and by 0421 UTC, almost no precipitation is detected by the NWRT PAR. A weak temperature increase of 1°C was detected at MEDI (Fig. 11), but no dew point depression was observed. Also, gusty winds were observed at MEDI after the evaporation was detected. Thus, the Mesonet data do not provide indications of a heat burst at MEDI. However, radar data may provide clues to what caused the evaporation to the northeast, and why a heat burst was not observed at the Mesonet site.

NWRT PAR and KTLX reflectivity (Fig. 12) show that from 0410-0414 UTC, a 40 dBZ core descends rapidly and dissipates. During this period, the evaporation intensifies, and the dry region becomes well-defined by 0418 UTC. Both signatures indicate that a microburst was likely during this period, and this microburst possibly induced a heat burst to the northeast of MEDI. Both KTLX and NWRT PAR detected the microburst and associated evaporation, but the depth of the dry region was better resolved by NWRT PAR. This is due to NWRT PAR scanning the region with four overlapped elevation scans versus KTLX using two non-overlapped scans. At 0413 UTC, KTLX shows that MEDI may be impacted by the evaporation, but PAR shows that at 0412 and 0414 UTC, the site remains just outside the affected area. In this case, PAR data shows that MEDI did not experience a heat burst, but one may have occurred only a few kilometers away.

Storm-relative velocity (Fig. 13) also provides indications of why the drying occurred during this heat burst. Both KTLX and PAR show that outflow slanted toward the ground as it advanced outward from the precipitation core. Descending flow indicates a region where a heat burst may develop if it reaches the surface. While KTLX does not indicate much evolution in the position or structure of the outflow, PAR returns show that the outflow above MEDI (white dot) approaches the ground between 0408 and 0412 UTC. As this flow advanced eastward, the region of evaporating precipitation became evident on both PAR reflectivity and velocity (0414–0419 UTC), indicating a heat burst may be ongoing. Meanwhile, KTLX did not detect drying on storm-relative velocity until 0417 UTC, approximately 5 min after PAR first detected the evaporation. NWRT PAR also detects near-surface divergence after 0417 UTC, while KTLX does not detect this signature. Thus, the NWRT PAR dense sampling strategy provided additional information to show that a microburst likely generated a heat burst in this case.

After 0500 UTC, another heat burst was sampled by PAR at El Reno, Oklahoma (ELRE; Fig. 14). Two different PAR scanning strategies were used to sample this heat burst. For a period between 0430 and 0505 UTC, 14 widely spaced elevation scans were used to obtain a fast temporal update rate at the expense of reduced vertical resolution (Heinselman et al. 2009). After 0505 UTC, the dense vertical strategy was used to obtain additional vertical resolution at a slower update rate.

Fig. 15, shows that the sparse elevation scans (panel a) provided limited details on the depth and structure of the stratiform region. Beam gaps obscured some of the precipitation features, including the depth and structure of the stratiform region. By switching to the dense sampling strategy (panel b), the depth of the stratiform region becomes well-defined. Also, a region of 10–15 dBZ reflectivity was observed by both scans, but the dense sampling strategy provides more information on the region's structure and depth. Since weak reflectivity echoes may indicate the location of heat bursts, the improved vertical sampling may provide additional indications that heat bursts were ongoing over a 5–10 km spatial region including ELRE. This information may be critical when surface observations are not available at a given location.

Storm-relative velocity from the two NWRT PAR strategies is compared in Fig. 16. In panel a, beam gaps obscure an apparent transition between the top of the rear-inflow and storm-relative outflow at 7–8 km AGL. The dense strategy (panel b) fills in these beam gaps, providing a clearer picture of the rear-inflow and outflow structures. Both scans demonstrate an ongoing rear-inflow heat burst, but the higher resolution of the dense scan shows a clear transition from storm-relative inflow at 5 km AGL to outflow near the ground. Also, the dense scan shows that near-surface outflow extended across a 10-km region, while the sparse strategy shows outflow over a smaller region. Thus, while both the sparse and dense scans detect a heat burst signature, the dense strategy provides a sharper definition of its structure. This information would be helpful when issuing warnings for surface locations that may be affected.

7. CONCLUSIONS

In this paper, we explored the impacts of vertical elevation spacing on the depiction of heat bursts occurring on 13 May 2009 over the Texas panhandle and southwest and western Oklahoma. Two WSR-

88Ds used standard VCPs to scan the storms, while the NWRT PAR used a dense vertical sampling strategy with 25 closely spaced elevation scans. Both types of radar detected heat burst signatures, but the closely spaced elevations used by PAR provided additional detail on heat burst structure. In the future, forecasters may use this information to provide improved forecasts of location, timing and severity of winds and temperature jumps that may occur with heat burst events.

To improve understanding of heat burst activity and corresponding radar signatures, we will examine the magnitude of reflectivity and velocity returns. Maximum values of reflectivity will be used to analyze the precipitation structure in the vicinity of each observed heat burst. Also, maximum and minimum storm-relative velocity will be analyzed to determine the magnitude of convergence or divergence observed. This information will help provide information on heat burst strength and the potential for severe winds at the surface. In cases where surface observations are not available, radar observations could provide insight into the severity and potential length of a heat burst. Forecasters could use this information to provide advanced warning to the public, potentially reducing the risk for damage or injury from severe winds or excessive heat.

8. ACKNOWLEDGEMENTS

This research was supported by grant #105099900 from NOAA / National Severe Storms Laboratory. Radar graphics were created using WDSS-II, a trademark of the University of Oklahoma. Surface observations in WDSS-II were obtained from the Oklahoma Mesonet, which is a trademark of the Oklahoma Climatological Survey.

References

Bernstein, B. C. and R. H. Johnson, 1994: A Dual-Doppler radar study of an OK PRE-STORM heat burst event. *Mon. Wea. Rev.*, **122**, 259–273.

Federal Meteorological Handbook, 2009: Doppler radar meteorological observations. Part A: System concepts, responsibilities, and procedures. Technical Report FCM-H11A-2009, Office of the Federal Coordinator for Meteorological Services and Supporting Research, Washington, DC, 53 pp.

Heinselman, P. L., S. M. Torres, R. Adams, C. D. Curtis, E. Forren, I. R. Ivic, D. Priegnitz, J. Thompson, and D. A. Warde, 2009: Phased array radar innovative sensing experiment. Preprints*, 34th Conference on Radar Meteorology*, Amer. Meteor. Soc., Williamsburg, VA, P6.5A.

Johnson, B. C., 1983: The heat burst of 29 May 1976. *Mon. Wea. Rev.*, **111**, 1776–1792.

Johnson, R. H., 2001: Surface mesohighs and mesolows. *Bull. Amer. Meteor. Soc.*, **82**, 13–31.

Lakshmanan, V., T. Smith, G. Stumpf, and K. Hondl, 2007: The Warning Decision Support System – Integrated Information. *Wea. Forecast.*, **22**, 596–612.

MacKeen, P. L., D. L. Andra, and D. A. Morris, 1998: The 22-23 May 1996 heatburst: A severe wind event. Preprints*, 19th Conference on Severe Local Storms*, Amer. Meteor. Soc., Minneapolis, MN, P11.13.

McPherson, R. A., K. C. Crawford, J. D. Lane, and W. G. McPherson, 2008: A climatology of heatbursts as detected by the Oklahoma Mesonet. Preprints*, 17th Conf. on Applied Climatology*, Amer. Meteor. Soc., Whistler, BC, 1.4.

McPherson, R. A., C. A. Fiebrich, K. C. Crawford, R. L. Elliott, J. R. Kilby, D. L. Grimsley, J. E. Martinez, J. B. Basara, B. G. Illston, D. A. Morris, K. A. Kloesel, S. J. Stadler, A. D. Melvin, A. J. Sutherland, H. Shrivastava, J. D. Carlson, J. M. Wolfinbarger, J. P. Bostic, and D. B. Demko, 2007: Statewide monitoring of the mesoscale environment: A technical update on the Oklahoma Mesonet. *J. Atmos. Ocean. Tech.*, **24**, 301–321.

National Academies, 2008: Evaluation of the Multifunction Phased Array Radar planning process. Technical report, Report prepared by the National Research Council, National Academy of Science, National Academy Press, 79 pp.

Sensi, J., 1988: The AEGIS system. *Aspects of Modern Radar*, E. E. Brookner, ed., Artech House, 239–251.

Weadon, M., P. Heinselman, D. Forsyth, W. E. Benner, G. S. Torok, and J. Kimpel, 2009: Multifunction Phased Array Radar. *Bull. Amer. Meteor. Soc.*, **90**, 385–389.

Wilson, J. W., R. D. Roberts, C. Kessinger, and J. McCarthy, 1984: Microburst wind structure and evaluation of Doppler radar for airport wind shear detection. *J. Climate Appl. Meteor.*, **23**, 898–915.

Zrnic, D. S., J. F. Kimpel, D. E. Forsyth, A. Shapiro, G. Crain, R. Ferek, J. Heimmer, W. Benner, T. J. McNellis, and R. J. Vogt, 2007: Agile-Beam phased array radar for weather observations. *Bull. Amer. Meteor. Soc.*, **88**, 1753–1766.

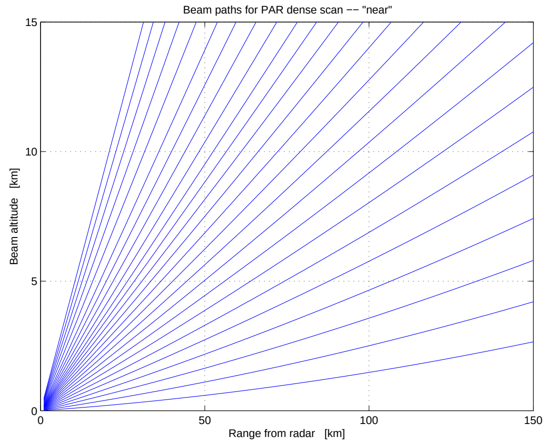

Figure 1. Beam paths in range and altitude for the dense scanning strategy – “near” scan. Additional information is presented in Table 1.

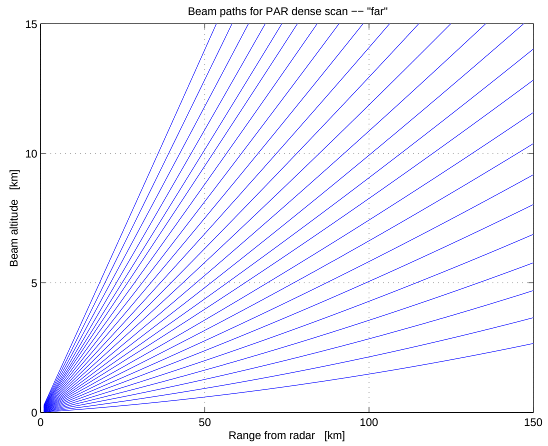

Figure 2. Same as Fig. 1, except displaying the “far” scan. More details are available in Table 2.

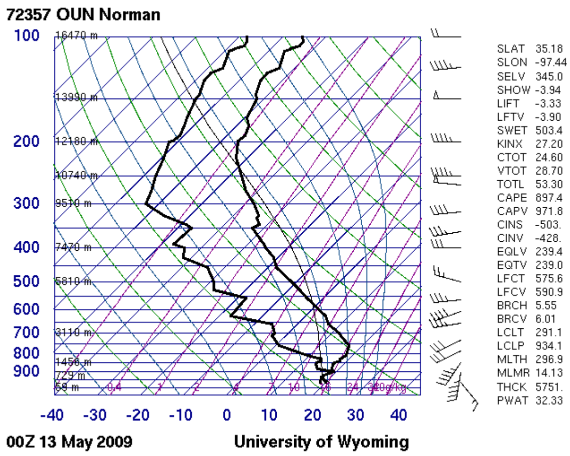

Figure 3. A sounding obtained from Norman, Oklahoma at 0000 UTC on 13 May 2009 (courtesy University of Wyoming).

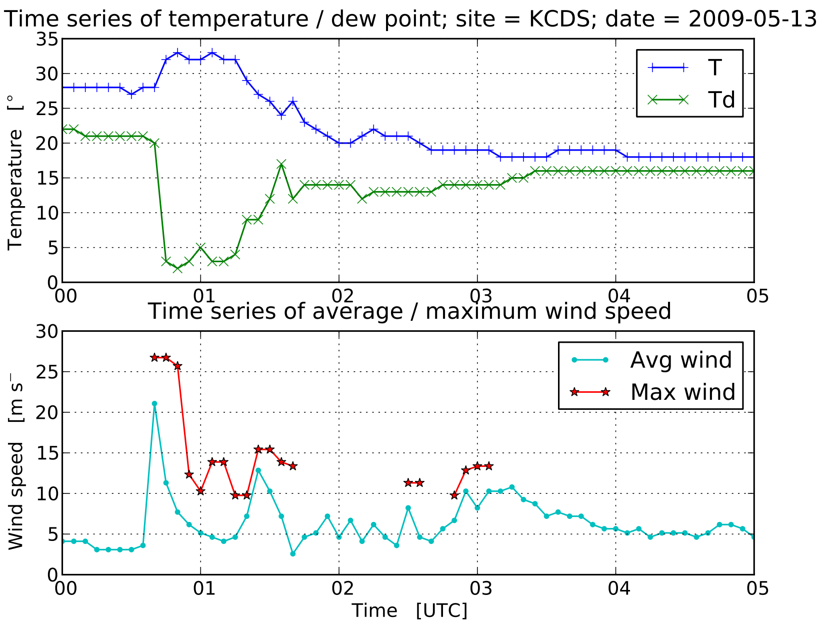

Figure 4. A time series of ASOS observations obtained from Childress, Texas (KCDS) on 13 May 2009. The top panel displays temperature and dew point temperature, while the bottom panel shows 5-min averaged winds. Maximum wind gusts are also displayed when available.

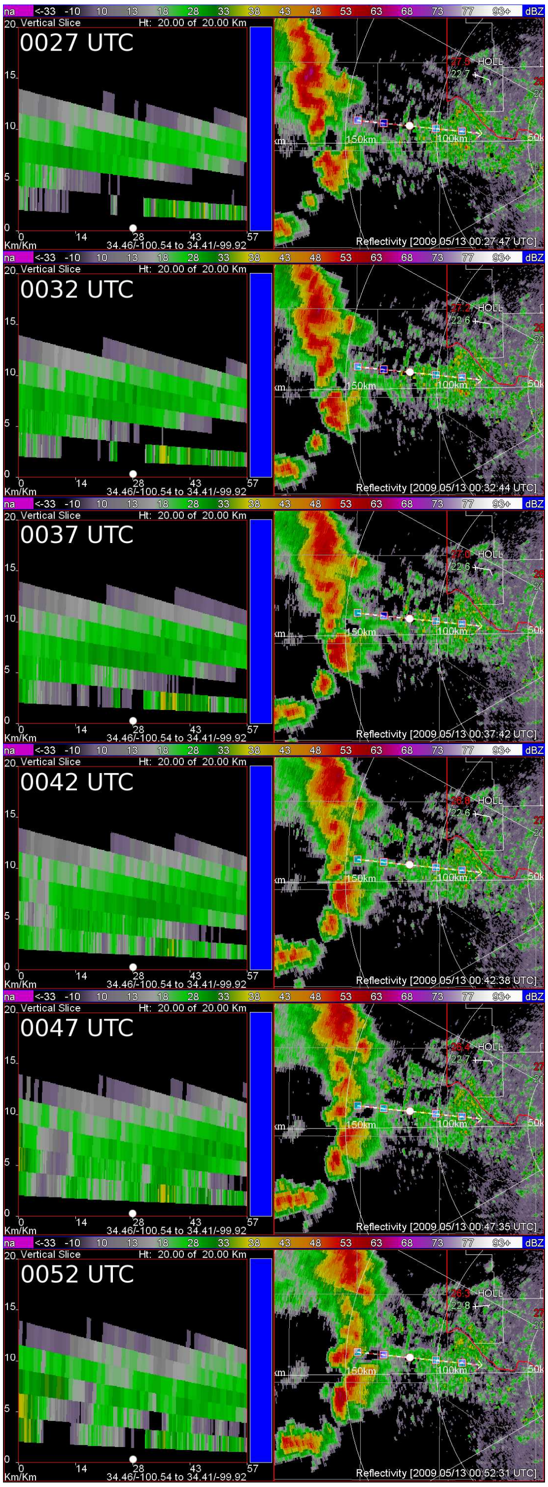

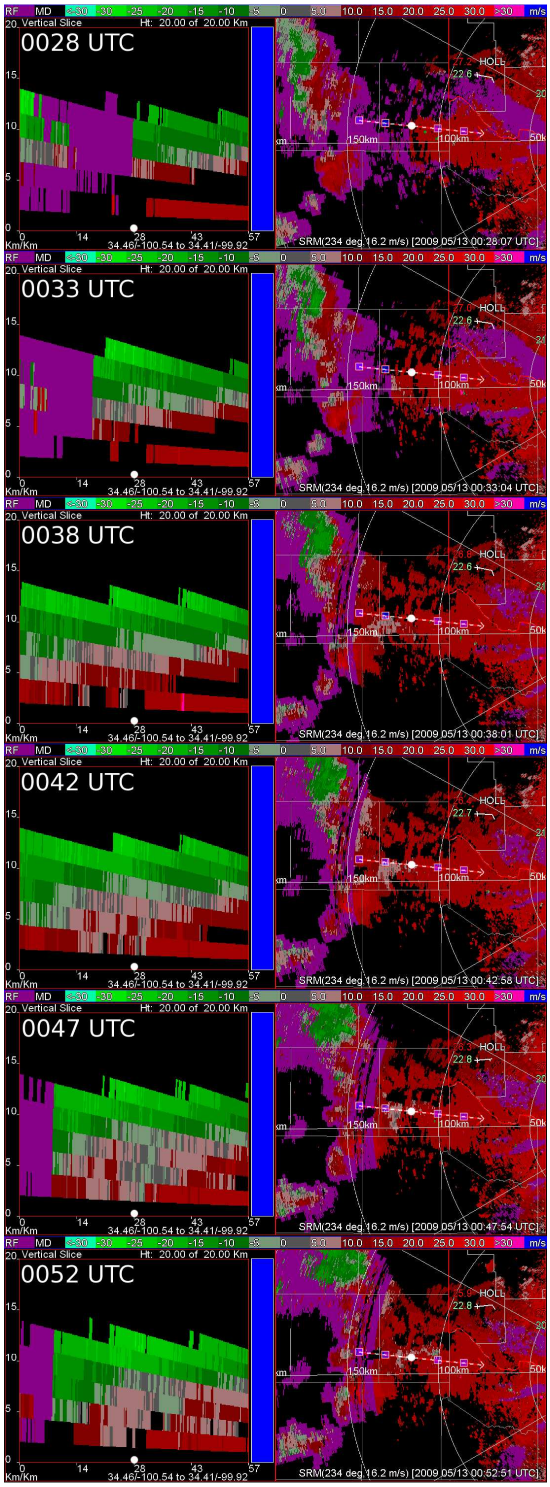

Figure 5. A series of reflectivity cross sections (left) and 0.5° PPI images (right) from the Frederick, Oklahoma (KFDR) WSR-88D on 13 May 2009. A strong heat burst is ongoing at Childress, Texas (KCDS) during this period. The location of KCDS is displayed as a white dot. Range rings are denoted on the PPI images in 50 km increments.

Figure 6. Same as Fig. 5, except showing storm-relative velocity.

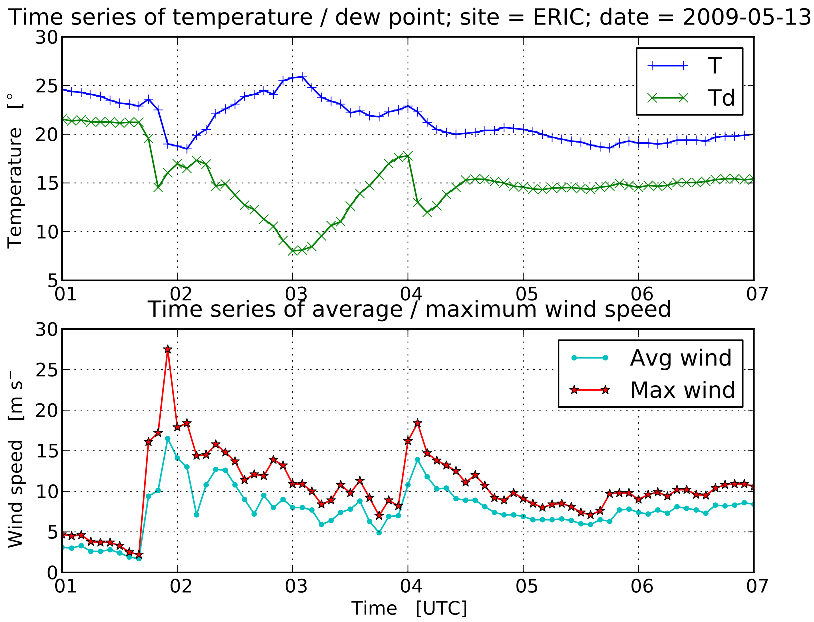

Figure 7. Oklahoma Mesonet time series obtained from Erick, Oklahoma (ERIC) on 13 May 2009. The top panel displays temperature and dew point temperature, while the bottom panel shows 5 min averaged wind speed and maximum wind gusts.

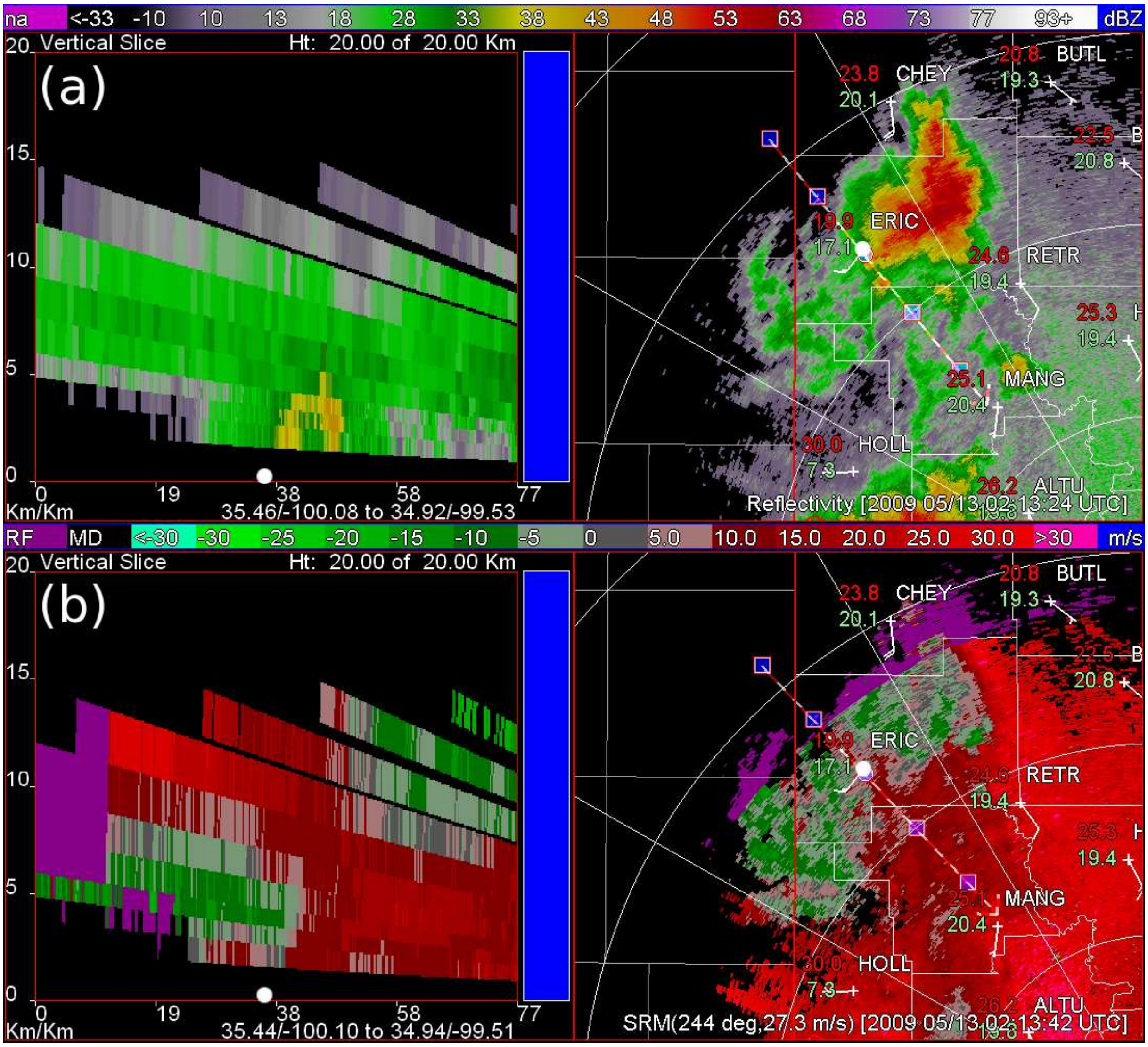

Figure 8. (a) A vertical cross-section and PPI of reflectivity obtained from KFDR at 0213 UTC. This scan was obtained during a 45-min sustained heat burst observed at Erick, Oklahoma (ERIC). A white dot indicates the location of ERIC on the PPI and cross section. (b) Same as (a), except displaying storm-relative velocity.

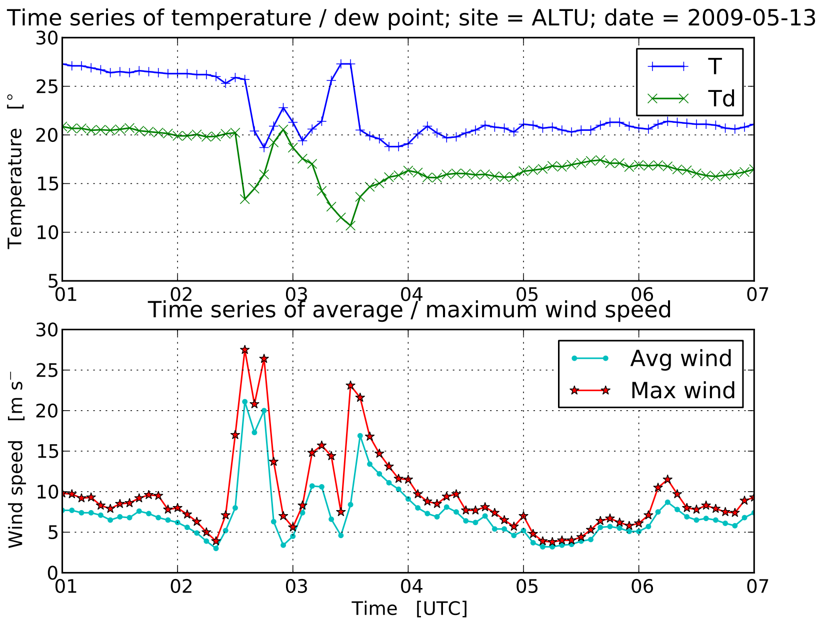

Figure 9. Same as Fig. 7, except displaying Mesonet data for Altus, Oklahoma (ALTU).

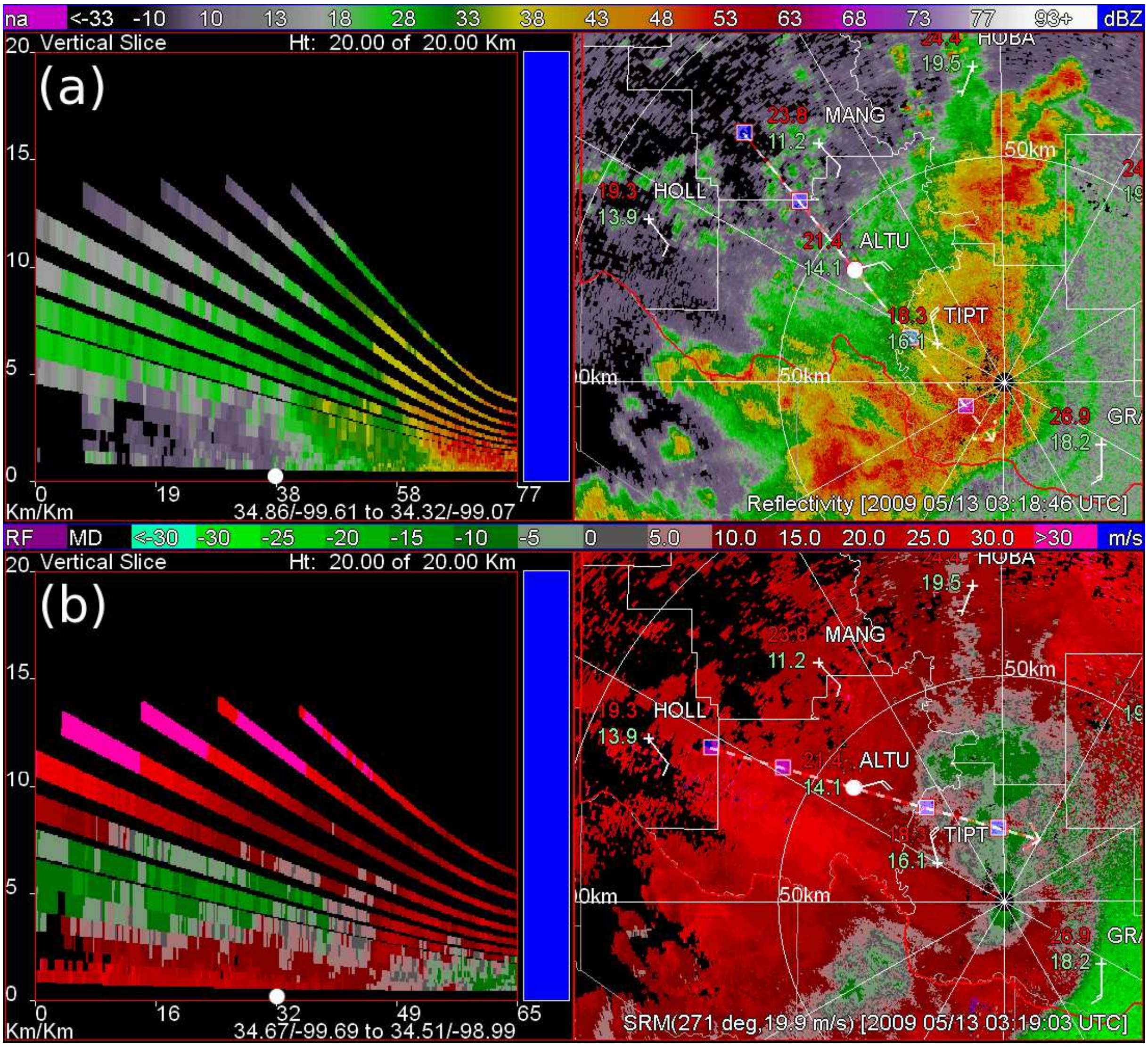

Figure 10. (a) A vertical cross-section and PPI of reflectivity obtained from KFDR at 0318 UTC as a heat burst is observed at Altus, Oklahoma (ALTU). A white dot indicates the location of ALTU on each image. (b) Same as (a), except displaying storm-relative velocity.

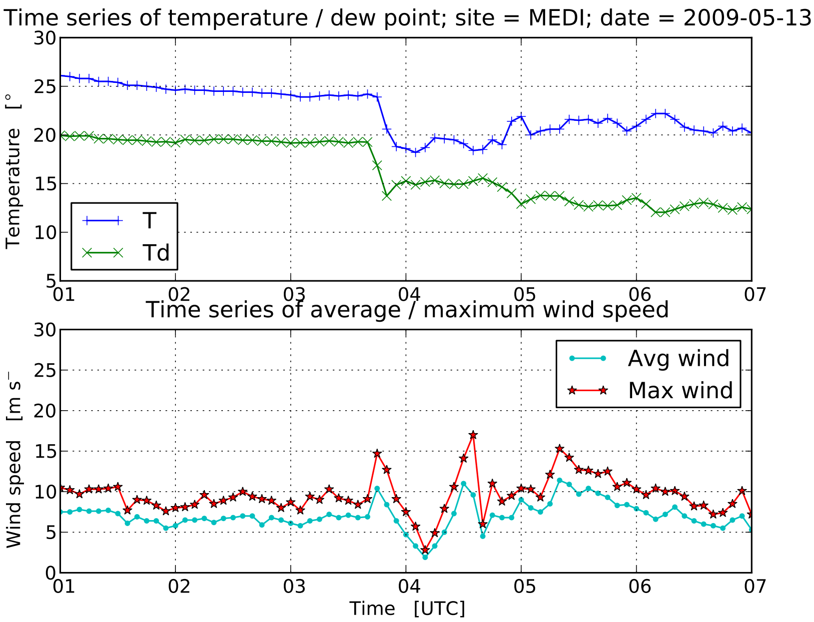

Figure 11. Same as Fig. 9, except displaying Mesonet data for Medicine Park, Oklahoma (MEDI).

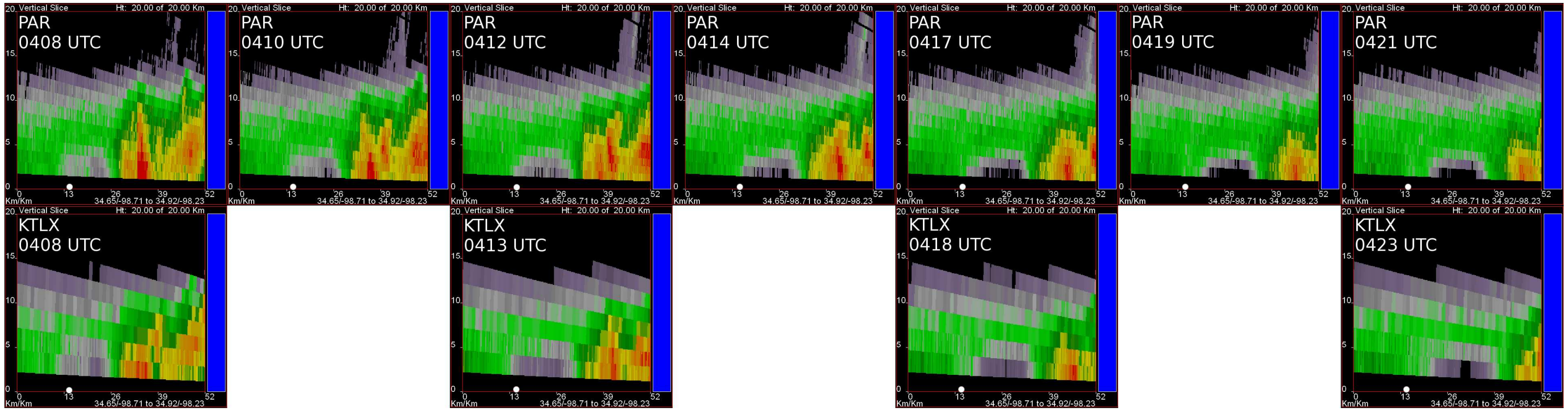

Figure 12. A series of reflectivity cross sections from PAR (top) and KTLX (bottom) during an observed heat burst at Medicine Park, Oklahoma (MEDI). Time stamps are indicated for each frame. A white dot indicates the location of MEDI on each panel.

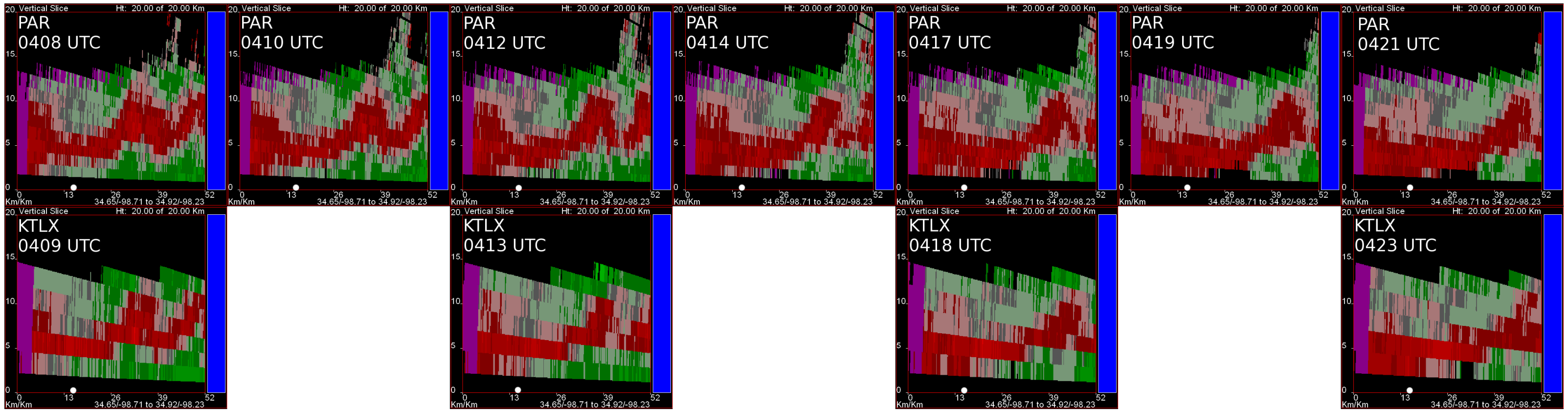

Figure 13. Same as Fig. 12, except displaying storm-relative velocity.

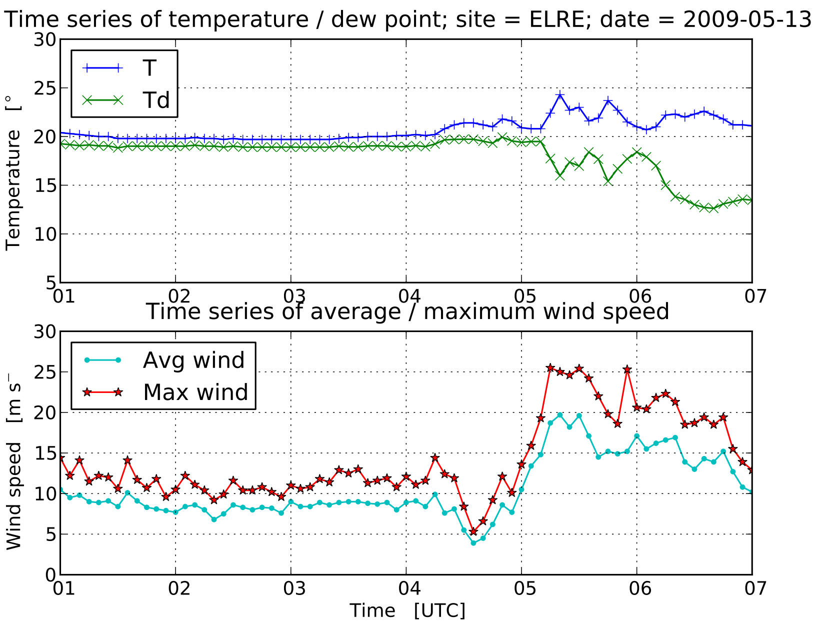

Figure 14. Same as Fig. 9, except displaying Mesonet data for El Reno, Oklahoma (ELRE).

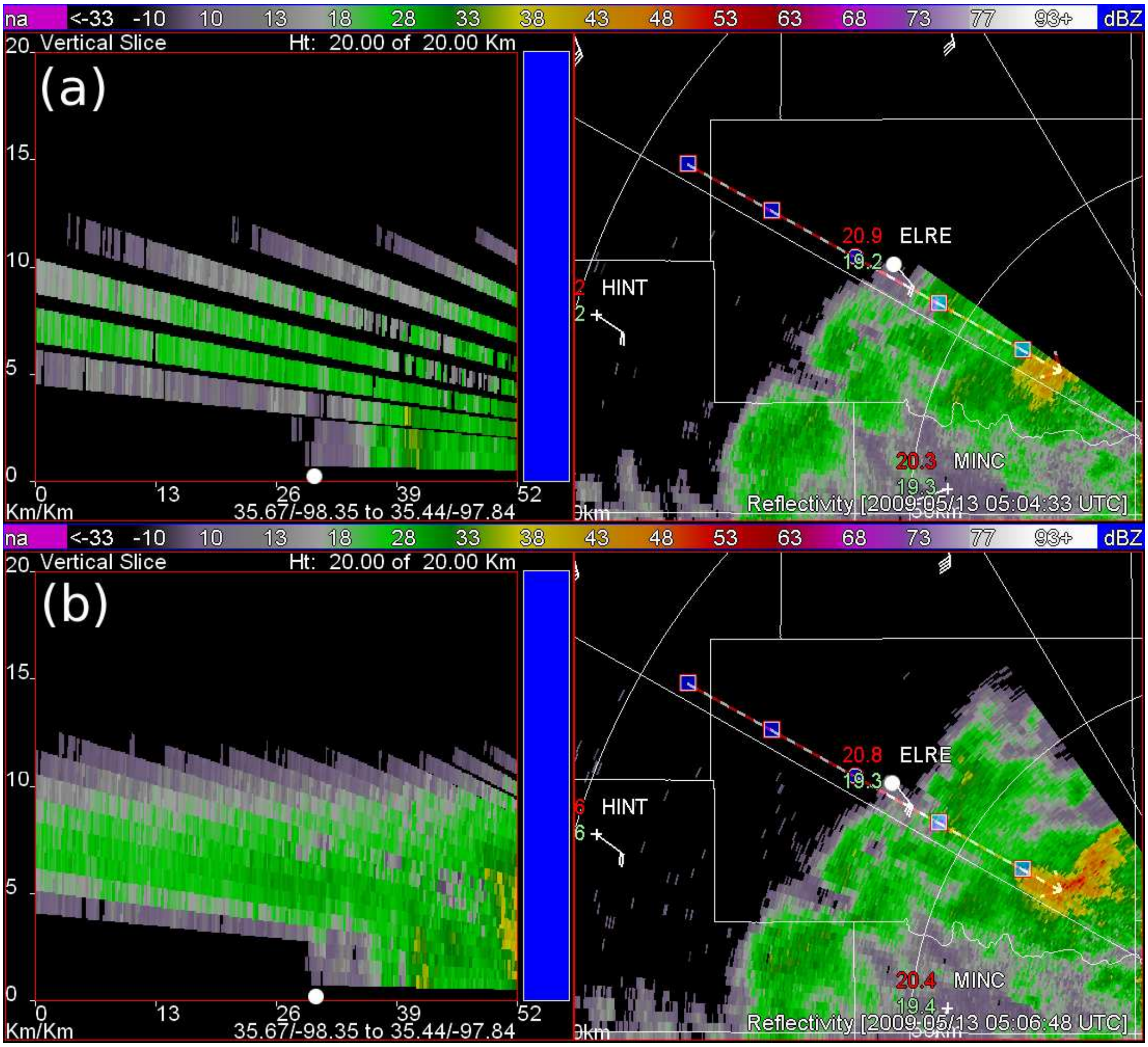

Figure 15. (a) A vertical cross-section and 0.5^o PPI scan obtained from PAR at 0504 UTC. A scanning strategy containing widely spaced elevation scans was used to obtain this data. A white dot indicates the location of ELRE on each image. (b) Same as (a), except displaying PAR reflectivity at 0506 UTC. Here, the dense vertical sampling strategy was used to obtain the volume scan.

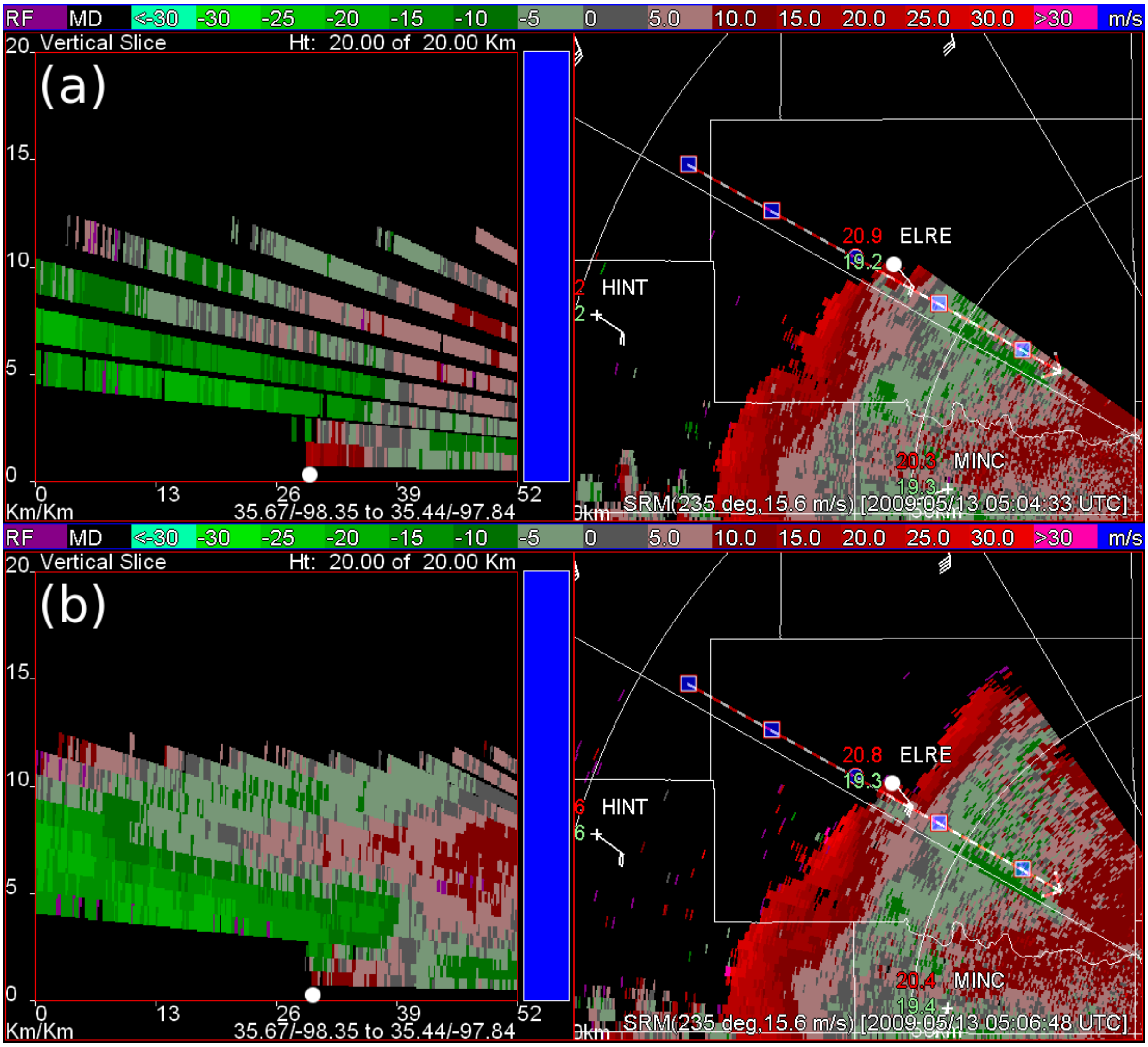

Figure 16. Same as Fig. 15, but displaying storm-relative velocity at (a) 0504 UTC and (b) 0506 UTC.

Table 1: Elevation angles (degrees) used for the dense scanning strategy – "near" scan. Legend: CS – Continuous Surveillance; CD – Continuous Doppler

Elevation (^{o})	Scan type	CS PRT (μs)	CS pulses (#)	CD PRT (μs)	CD pulses (#)	Nyquist vel (m s^{-1})	CS R_{max} (km)	CD R_{max} (km)
0.51	CS	3104	17				465.6	
0.51	CD			904	44	25.9		135.6
1.10	CS	3104	17				465.6	
1.10	CD			904	44	25.9		135.6
1.71	CS	2704	17				405.6	
1.71	CD			904	44	25.9		135.6
2.33	CS	2304	17				345.6	
2.33	CD			904	44	25.9		135.6
2.97	CS	2000	17				300.0	
2.97	CD			904	44	25.9		135.6
3.61	CS	1800	17				270.0	
3.61	CD			904	44	25.9		135.6
4.27	CS	1600	17				240.0	
4.27	CD			904	44	25.9		135.6
4.93	CS	1400	17				210.0	
4.93	CD			904	44	25.9		135.6
5.61	CS	1200	17				180.0	
5.61	CD			904	44	25.9		135.6
6.30	CS	1200	17				180.0	
6.30	CD			904	44	25.9		135.6
7.00	CD			904	45	25.9		135.6
7.72	CD			800	45	29.3		120.0
8.46	CD			800	45	29.3		120.0
9.22	CD			800	45	29.3		120.0
10.00	CD			800	45	29.3		120.0
10.80	CD			800	45	29.3		120.0
11.80	CD			800	45	29.3		120.0
13.00	CD			800	45	29.3		120.0
14.40	CD			800	45	29.3		120.0
16.00	CD			800	45	29.3		120.0
18.30	CD			800	45	29.3		120.0
20.70	CD			800	45	29.3		120.0
23.20	CD			800	45	29.3		120.0
25.80	CD			800	45	29.3		120.0
28.50	CD			800	45	29.3		120.0

Total scan time (60^o sector): 77.4 s

Total scan time (90^o sector): 116.2 s

Azimuth width: 1.0^o

Table 2: Elevation angles (degrees) used for the dense scanning strategy – “far” scan. Legend: CS – Continuous Surveillance; CD – Continuous Doppler

Elevation (^{o})	Scan type	CS PRT (μs)	CS pulses (#)	CD PRT (μs)	CD pulses (#)	Nyquist vel (m s^{-1})	CS R_{max} (km)	CD R_{max} (km)
0.51	CS	3104	17				465.6	
0.51	CD			904	40	25.9		135.6
0.89	CS	3104	17				465.6	
0.89	CD			904	40	25.9		135.6
1.29	CS	3000	17				450.0	
1.29	CD			904	40	25.9		135.6
1.70	CS	2704	17				405.6	
1.70	CD			904	40	25.9		135.6
2.12	CS	2504	17				375.6	
2.12	CD			904	40	25.9		135.6
2.56	CS	2200	17				330.0	
2.56	CD			904	40	25.9		135.6
3.00	CS	2000	17				300.0	
3.00	CD			904	40	25.9		135.6
3.46	CS	1800	17				270.0	
3.46	CD			904	40	25.9		135.6
3.92	CS	1648	17				247.2	
3.92	CD			904	40	25.9		135.6
4.40	CS	1504	17				225.6	
4.40	CD			904	40	25.9		135.6
4.86	CS	1400	15				210.0	
4.86	CD			904	40	25.9		135.6
5.36	CS	1304	15				195.6	
5.36	CD			904	40	25.9		135.6
5.90	CS	1200	15				180.0	
5.90	CD			904	40	25.9		135.6
6.48	CS	1048	15				157.2	
6.48	CD			904	40	25.9		135.6
7.10	CD			904	40	25.9		135.6
7.76	CD			800	40	29.3		120.0
8.46	CD			800	40	29.3		120.0
9.20	CD			800	40	29.3		120.0
9.98	CD			800	40	29.3		120.0
10.80	CD			800	40	29.3		120.0
11.54	CD			800	40	29.3		120.0
12.44	CD			800	40	29.3		120.0
13.50	CD			800	40	29.3		120.0
14.72	CD			800	40	29.3		120.0
16.10	CD			800	40	29.3		120.0

Total scan time (60^o sector):	77.4 s
Total scan time (90^o sector):	116.1 s
Azimuth width:	1.0^o